

Non-equilibrium Ionization Effects on Extreme-Ultraviolet Emissions Modulated by Standing Sausage Modes in Coronal Loops

MIJIE SHI,^{1,2} BO LI,¹ TOM VAN DOORSSELAERE,³ SHAO-XIA CHEN,¹ AND ZHENGHUA HUANG¹

¹*Shandong Provincial Key Laboratory of Optical Astronomy and Solar-Terrestrial Environment, Institute of Space Sciences, Shandong University, Weihai 264209, China*

²*CAS Key Laboratory of Solar Activity, National Astronomical Observatories, Beijing 100012, China*

³*Centre for Mathematical Plasma Astrophysics, Department of Mathematics, Celestijnenlaan 200B, B-3001, KU Leuven, Leuven, Belgium*

(Received ****; Revised ****; Accepted ****)

ABSTRACT

Forward-modeling the emission properties in various passbands is important for confidently identifying magnetohydrodynamic waves in the structured solar corona. We examine how Non-equilibrium Ionization (NEI) affects the Extreme Ultraviolet (EUV) emissions modulated by standing fast sausage modes (FSMs) in coronal loops, taking the Fe IX 171 Å and Fe XII 193 Å emission lines as examples. Starting with the expressions for linear FSMs in straight cylinders, we synthesize the specific intensities and spectral profiles for the two spectral lines by incorporating the self-consistently derived ionic fractions in the relevant contribution functions. We find that relative to the case where Equilibrium Ionization (EI) is assumed, NEI considerably impacts the intensity modulations, but shows essentially no effect on the Doppler velocities or widths. Furthermore, NEI may affect the phase difference between intensity variations and those in Doppler widths for Fe XII 193 Å when the line-of-sight is oblique to the loop axis. While this difference is 180° when EI is assumed, it is ~ 90° when NEI is incorporated for the parameters we choose. We conclude that in addition to viewing angles and instrumental resolutions, NEI further complicates the detection of FSMs in spectroscopic measurements of coronal loops in the EUV passband.

Keywords: magnetohydrodynamics — Sun: corona — Sun: UV radiation — waves

1. INTRODUCTION

The past two decades have witnessed rapid developments of coronal seismology, thanks to the abundantly identified low-frequency waves and oscillations in the highly structured solar corona (see recent reviews by e.g., Nakariakov & Verwichte 2005; Banerjee et al. 2007; De Moortel & Nakariakov 2012; Nakariakov et al. 2016). However, identifying a measured oscillatory signal with a specific magnetohydrodynamic (MHD) wave mode is not straightforward. Take the deceptively simple case

of slow waves in coronal loops, and assume that the spatial dependence of the associated perturbations is restricted to the axial direction. Starting with an analytical model for the fluid parameters, the forward-modeling effort by [De Moortel & Bradshaw \(2008\)](#), and references therein) demonstrated that the periods in the modulated intensities in, say, Fe XII 195Å, do not necessarily correspond to the wave period, let alone the damping rates. This results from the intricate dependence of the emissivity on density and ionization balance. (See also [Ruan et al. 2016](#) for a more recent forward-modeling study on slow waves in the corona.) The situation becomes even trickier when one considers the distribution of wave perturbations transverse to coronal loops, because this further complicates the integration of emissivities along a Line-of-Sight (LoS). Fast sausage modes (FSMs) are the simplest in this regard because they are axisymmetric and hence avoid the additional complication associated with the azimuthal dependence (see e.g., [Yuan & Van Doorselaere 2016](#); [Antolin et al. 2017](#), for more discussions). A variety of forward-modeling studies have been conducted with different levels of sophistication, starting from the works by [Cooper et al. \(2003a\)](#) and [Cooper et al. \(2003b\)](#) who computed the modulated intensities by integrating squared densities along LoS with different viewing angles. This approach was taken further by [Gruszecki et al. \(2012\)](#) who examined the effects of spatial resolution, namely the “width” of an LoS. Further incorporating the contribution function into the computations by assuming equilibrium ionization (EI), [Antolin & Van Doorselaere \(2013\)](#), hereafter AvD13) derived the spectral profiles of Fe IX 171 Å and Fe XII 193 Å emission lines. As found from this series of studies, the observability of FSMs in EUV emissions depends rather sensitively on such geometrical parameters as viewing angles, and on instrumental parameters like temporal and spatial resolutions as well.

Similar to AvD13, this study will also address the spectral properties of Fe IX 171 Å and Fe XII 193 Å as modulated by standing FSMs. New is that non-equilibrium ionization (NEI) is addressed when computing the ionic fractions of Fe IX and XII. The reason for doing this is that the periods of FSMs in coronal loops are determined by the transverse Alfvén time, which typically attains a couple of seconds (e.g., [Rosenberg 1970](#); [Zajtsev & Stepanov 1975](#); [Spruit 1982](#); [Edwin & Roberts 1983](#); [Cally 1986](#)). However, the ionization and recombination timescales for the relevant ionization states are comparable to, or even substantially longer than the wave period in the case of Fe XII (see Table 1 in AvD13). This means that in general the ionic fractions cannot respond instantaneously to the variations in the electron temperature, and differences from the EI computations are expected. To isolate the effects of NEI, we will examine the simplest configuration where FSMs are hosted by a straight, axially homogeneous cylinder with physical parameters distributed in a piece-wise constant manner transverse to the cylinder. By doing this, we are avoiding the complications due to the continuous transverse structuring (e.g., [Nakariakov et al. 2012](#); [Li et al. 2014](#); [Chen et al. 2015b, 2016](#); [Cally & Xiong 2018](#)). In addition, we will focus only on trapped modes such that no apparent attenuation is involved. Section 2 will formulate the FSMs and describe the equilibrium parameters, and Section 3 will describe how the emission properties are computed. We will present our results in Section 4 before concluding this study in Section 5.

2. LINEAR STANDING FAST SAUSAGE MODES IN CORONAL LOOPS

We model an equilibrium coronal loop as a static, straight cylinder with radius $R = 1.5 \times 10^3$ km and length-to-radius ratio $L/R = 12.5$. In a cylindrical coordinate system (r, ϕ, z) , both the cylinder axis and the equilibrium magnetic field \mathbf{B} are in the z -direction. We adopt single-fluid ideal MHD and consider an electron-proton plasma throughout. The equilibrium parameters are structured only

in the r -direction, and subscript i (e) denotes the constant values inside (outside) the cylinder. Let N , T , and B denote the electron number density, electron temperature, and magnetic field strength, respectively. We take $[N_i, N_e] = [5, 0.5] \times 10^9 \text{ cm}^{-3}$, and $[T_i, T_e] = [1, 0.74] \text{ MK}$. We further take $B_i = 16.2 \text{ G}$, and hence an external one $B_e = 17.2 \text{ G}$ results from transverse force balance. For reference, the internal (external) plasma beta is $\beta_i = 0.13$ ($\beta_e = 0.009$). Furthermore, the Alfvén speed in the internal (external) medium reads $v_{Ai} = 500$ ($v_{Ae} = 1675$) km s^{-1} .

In this equilibrium, standing linear FSMs perturb all physical parameters except the azimuthal components of the velocity and magnetic field. Suppose that the system has reached a stationary state characterized by angular frequency ω and axial wavenumber k . The physical variables relevant for computing EUV emissions are given by

$$N(r, z; t) = N_0[1 - \mathcal{D}(r) \sin(\omega t) \sin(kz)] , \quad (1)$$

$$v_r(r, z; t) = \omega \mathcal{R}(r) \cos(\omega t) \sin(kz) , \quad (2)$$

$$v_z(r, z; t) = -\frac{c_s^2}{\omega/k} \mathcal{D}(r) \cos(\omega t) \cos(kz) , \quad (3)$$

$$T(r, z; t) = T_0[1 - (\gamma - 1)\mathcal{D}(r) \sin(\omega t) \sin(kz)] , \quad (4)$$

where both the equilibrium values (subscript 0) and perturbations are involved, and $\gamma = 5/3$ is the adiabatic index. Here \mathcal{R} denotes the transverse (i.e., radial) profile of the transverse Lagrangian displacement as given by

$$\mathcal{R}(r) = \begin{cases} ARJ_1(nr) , & r < R , \\ \frac{ARJ_1(nR)}{K_1(mR)} K_1(mr) , & r > R , \end{cases} \quad (5)$$

where the constant A determines the relative magnitude, and J_1 (K_1) is the Bessel function of the first kind (modified Bessel function of the second kind). In addition, the effective transverse wavenumbers n and m are defined by

$$n^2 = \frac{(\omega^2 - k^2 v_{Ai}^2)(\omega^2 - k^2 c_{si}^2)}{(c_{si}^2 + v_{Ai}^2)(\omega^2 - k^2 c_{Ti}^2)} ,$$

$$m^2 = -\frac{(\omega^2 - k^2 v_{Ae}^2)(\omega^2 - k^2 c_{se}^2)}{(c_{se}^2 + v_{Ae}^2)(\omega^2 - k^2 c_{Te}^2)} ,$$

where c_s and $c_T = c_s v_A / \sqrt{c_s^2 + v_A^2}$ are the adiabatic sound and tube speeds, respectively¹. For an electron-proton plasma, $c_s^2 = 2\gamma k_B T_0 / m_p$ with k_B being the Boltzmann constant and m_p the proton mass. As for \mathcal{D} , it is related to \mathcal{R} by

$$\mathcal{D}(r) = \frac{\omega^2}{\omega^2 - k^2 c_s^2} \frac{d(r\mathcal{R})}{r dr} . \quad (6)$$

¹ We use Bessel's K function to describe the perturbations outside the tube because we will examine trapped modes. In this case ω is real-valued, n^2 and m^2 are both non-negative (see e.g., Cally 1986; Kopylova et al. 2007; Chen et al. 2015b, 2016, for more discussions on this aspect).

For future reference, we note that the Lagrangian displacements in the radial and axial directions are given by

$$\xi_r(r, z; t) = \mathcal{R}(r) \sin(\omega t) \sin(kz) , \quad (7)$$

$$\xi_z(r, z; t) = -\frac{c_s^2}{\omega^2/k} \mathcal{D}(r) \sin(\omega t) \cos(kz) , \quad (8)$$

Finally, the angular frequency ω is found by solving the relevant dispersion relation (e.g., [Edwin & Roberts 1983](#), Eq. 8b).

We adopt the following parameters for the perturbations. The axial wavenumber k is taken to be $5\pi/L$, corresponding to the fourth longitudinal harmonic. Solving the dispersion relation then yields a wave period $P = 2\pi/\omega$ of 6.21 secs for the transverse fundamental mode, which is in the trapped regime. Consequently, the axial phase speed ω/k reads $2.41 v_{\text{Ai}} = 1207 \text{ km s}^{-1}$. The relative magnitude of the transverse displacement (A) is specified such that the peak value in v_r is $0.06 v_{\text{Ai}} = 30 \text{ km s}^{-1}$. The transverse displacement ξ_r can reach up to $0.02R = 30 \text{ km}$. The peak value in the perturbed density (temperature) reads $\sim 0.09N_i$ ($\sim 0.06T_i$). As for the axial velocity, the peak value is only $\sim 0.0041 v_{\text{Ai}}$ (2.07 km s^{-1}), which is readily understandable because of the factor in front of \mathcal{D} in Equation (3).

We now construct the spatial distributions of the fluid parameters in the $r - z$ plane with a spacing of 30 km in both directions for t between 0 and 4 periods. While this is implemented on a Eulerian grid, we take advection into account by assigning, to a point \mathbf{x} at time t , the physical parameters evaluated at $\mathbf{x}' = \mathbf{x} - \xi(\mathbf{x}, t)$ where ξ is the displacement vector ². Figure 1 presents the spatial distributions in a cut, through the cylinder axis, of the fluid parameters at some representative instants of time. The radial (v_r) and axial (v_z) speeds are shown for $t = 0$, while the electron density (N) and temperature (T) are displayed for $t = P/4$. From Figures 1c and 1d, one can barely discern the expansion or contraction of the coronal tube. Different instants of time are chosen due to the $\pi/2$ phase difference between the relevant perturbations (see Equations 1 to 4). In Figure 1a, the white dashed lines denote two lines-of-sight that both pass through the cylinder axis. Let θ denote the angle between a LoS and the cylinder axis. Then the LoS labeled 1 (2) corresponds to a θ being 0° (45°), chosen to represent normal (oblique) viewing angles that one frequently encounters in observations.

3. COMPUTING EMISSION MODULATIONS DUE TO SAUSAGE MODES

The coupled equations governing the ionic fraction (f_q) for Fe of charge state q are given by

$$\left(\frac{\partial}{\partial t} + \mathbf{v} \cdot \nabla \right) f_q = N [f_{q-1}C_{q-1} - f_q(C_q + R_q) + f_{q+1}R_{q+1}] , \quad (9)$$

where the ionization (C) and recombination (R) rate coefficients depend only on electron temperature T and are found with CHIANTI (ver 8, [Del Zanna et al. 2015](#)) ³. If neglecting the left-hand side (LHS), or equivalently assuming that the wave period is much longer than the ionization timescales, then we end up with a set of coupled algebraic equations that pertain to EI, namely ionization balance. By noting that there is no Fe 0 or Fe XXVIII, one finds that the rate of ionization into q

² In principle, \mathbf{x}' should be computed such that $\mathbf{x}' + \xi(\mathbf{x}', t) = \mathbf{x}$. But the difference between the two sets of values for \mathbf{x}' is $\xi \cdot \nabla \xi$ and therefore of second-order.

³ <http://www.chiantidatabase.org/>

balances the rate of recombination out of q . In other words,

$$C_{q-1}f_{q-1} = R_q f_q . \quad (10)$$

In reality, the wave period is not necessarily much longer than the ionization timescales. To take NEI into account, we then solve Equation (9) at each Eulerian grid point by initiating the solution procedure with the EI solution at time $t = 0$. The integration procedure is similar to earlier works (e.g., Ko et al. 2010; Shen et al. 2013) in other contexts. It suffices to consider only Fe V to XV, because the fractions of the rest of ionic states are negligible. The time step for integrating Equation (9) is small enough to resolve the ionization or recombination processes, and we make sure that $\left| \sum_{q=V}^{XV} f_q - 1 \right| < 10^{-5}$.

Figure 2 displays the temporal evolution of the ionic fractions of Fe IX (f_{IX} , Fig. 2b) and Fe XII (f_{XII} , Fig. 2c) at $[r, z] = [0, L/2]$, where the compressibility is the strongest. In addition to the NEI results (the blue curves), their EI counterparts are also shown (red). The temporal evolution of the electron temperature (T) at the same location is presented in Figure 2a for reference. As expected, the ionic fractions respond instantaneously to the variation in T in the equilibrium case. In particular, one sees that f_{IV} (f_{XII}) is in anti-phase (in-phase) with T for the parameters considered. This behavior can be understood as follows, for which purpose we define $\Gamma_q = C_{q-1}/R_q$ and $\Pi_q = \Gamma_1 \Gamma_2 \cdots \Gamma_q$. Note that Γ_1 is defined to be unity. Then the algebraic equations pertaining to EI (Equation 10) yield that

$$f_I = \frac{1}{\Pi_1 + \Pi_2 + \cdots + \Pi_{27}} , \quad (11)$$

$$f_q = f_{q-1} \Gamma_q = f_I \Pi_q \quad \text{for } q \geq 2 . \quad (12)$$

In agreement with physical intuitions, Γ_q decreases monotonically with q at a fixed T and increases monotonically with T at a fixed q . And it turns out that either Γ_9 or Γ_{10} is the last one that exceeds unity in the Γ_q series in the examined temperature range.⁴ Regardless, the fraction of Fe I in EI can be expressed as

$$f_I = \frac{1/\Pi_9}{1 + 1/\Gamma_9 + \Gamma_{10} + \Gamma_{10}\Gamma_{11} + \Gamma_{10}\Gamma_{11}\Gamma_{12} + \cdots} , \quad (13)$$

where we have neglected the terms represented by \cdots because they contribute no larger than 1%. Equation (12) then indicates that

$$f_{IX} = \frac{1}{1 + 1/\Gamma_9 + \Gamma_{10} + \Gamma_{10}\Gamma_{11} + \Gamma_{10}\Gamma_{11}\Gamma_{12} + \cdots} . \quad (14)$$

Now define $' = d/dT$ and let G_9 denote the denominator. One then finds that $f'_{IX} = (\Gamma'_9/\Gamma_9^2 - \Gamma'_{10} - \cdots)/G_9^2$. It turns out that the term associated with Γ_9 in the parentheses is at least a factor of ~ 7

⁴ Note that Γ_1 is defined to be unity for mathematical convenience, and only the series $\{\Gamma_2, \Gamma_3, \cdots, \Gamma_{27}\}$ is physically relevant. Note also that Γ_q depends on both q and the electron temperature (T). Taking the perturbation due to the fast sausage mode into account, we find that T varies between 0.736 and 1.061 MK. In this range, Γ_q ($q \leq 9$) is consistently larger than unity, whereas Γ_q ($q \geq 11$) is consistently smaller than unity. However, Γ_{10} exceeds unity only when $T \gtrsim 1.054$ MK. Now that Γ_q decreases with q at a fixed T , one finds that Γ_9 is the last element that exceeds unity in the $\{\Gamma_q\}$ series for $T \lesssim 1.054$ MK, and Γ_{10} takes up this role when $T \gtrsim 1.054$ MK. For instance, when $T = 1$ MK, one finds that $[\Gamma_8, \Gamma_9, \Gamma_{10}, \Gamma_{11}] = [21.3, 6.71, 0.817, 0.411]$. However, this series reads $[24.4, 7.85, 1.03, 0.5251]$ when $T = 1.06$ MK.

smaller than the rest in magnitude. Therefore f'_{IX} is always negative for the temperature range we examine, and hence an anti-phase behavior between f_{IX} and T . Moving on to the next ionic state Fe X, we find that f'_X is always positive. This can be understood with Equation (12), which leads to that $(\ln f_X)' = (\ln f_{\text{IX}})' + (\ln \Gamma_{10})'$. We find that $(\ln \Gamma_{10})'$ dominates $(\ln f_{\text{IX}})'$, and hence an f'_X that is always positive despite a negative f'_{IX} . From Fe XI onward, Equation (12) suggests that f'_q is positive definite because both f'_{q-1} and Γ'_q are positive. And hence the in-phase relationship between f_{XII} and T .

When NEI is incorporated, however, a time lag exists between the temperature and ionic fraction variations given the finite ionization and recombination timescales. The magnitude of variations in f is also weaker than in the EI case, which is true for both ionization states. Focusing on the NEI results, one finds that it takes about 4 secs for the ionic fractions to settle to a stationary state. In the first ~ 4 secs, the magnitude of f_{IX} (f_{XII}) decreases (increases) slightly with time. This behavior can be explained by Equation (9) as follows, which turns out to be rather involved. To start, the advection term $\mathbf{v} \cdot \nabla f_q$ turns out to be negligible throughout the entire computational domain. To see this, we note that this term is associated with a frequency $\mathbf{v} \cdot \nabla$, which is dominated by $v_r \partial / \partial r$. Replacing $\partial / \partial r$ with $1/R$ and noting that v_r reaches up to 30 km s^{-1} , one finds that $\mathbf{v} \cdot \nabla \sim 0.02 \text{ Hz}$, which is much smaller than $\omega = 2\pi/P = 1.01 \text{ rad s}^{-1}$. This makes f_q effectively local given that the right-hand side (RHS) of Equation (9) involves only the values evaluated at a given location. We neglect the advection term in the following discussions, and see f_q , N , C_q , and R_q as functions of t because we are examining a fixed location. Now define the ionization (ζ_C) and recombination (ζ_R) frequencies as

$$\zeta_{C,q} = N^{(0)} C_q^{(0)} , \quad (15)$$

$$\zeta_{R,q} = N^{(0)} R_q^{(0)} , \quad (16)$$

where the superscript 0 denotes the values at $t = 0$. Define further that

$$\Delta g(t) = g(t) - g^{(0)} , \quad (17)$$

where g denotes f_q , N , C_q , and R_q . Note that $\Delta f_q(t = 0) = 0$ by definition. Equation (9) then becomes ⁵

$$\begin{aligned} \frac{d\Delta f_q}{dt} &= \zeta_{C,q-1} \Delta f_{q-1} - (\zeta_{C,q} + \zeta_{R,q}) \Delta f_q + \zeta_{R,q+1} \Delta f_{q+1} \\ &\quad + \Delta_1 + \Delta_2 + \Delta_3 , \end{aligned} \quad (18)$$

where

$$\Delta_1 = N^{(0)} \left[f_{q-1}^{(0)} \Delta C_{q-1} - f_q^{(0)} (\Delta C_q + \Delta R_q) + f_{q+1}^{(0)} \Delta R_{q+1} \right] . \quad (19)$$

Furthermore, Δ_2 involves terms like $\Delta C_{q-1} \Delta f_{q-1}$ and $\Delta N \Delta C_{q-1}$, while Δ_3 involves such terms as $\Delta N \Delta C_{q-1} \Delta f_{q-1}$. It turns out that Δ_3 can be safely neglected but the same is not true for Δ_2 despite

⁵ The terms on the RHS of Equation (18) involve at least one symbol with Δ . This is because we initiate the solution procedure with the EI solution, meaning that $f_{q-1}^{(0)} C_{q-1}^{(0)} = f_q^{(0)} R_q^{(0)}$. While choosing this initial condition seems arbitrary, the solution procedure needs to be initiated at any rate and adopting the EI solution has been a common practice (e.g., Ko et al. 2010; Shen et al. 2013).

that we are actually examining linear waves. Nonetheless, we make two simplifications for tractability and see whether the approximate solutions are good enough afterwards. One is that Δ_2 and Δ_3 can be omitted from Equation (18). The other is that ΔC and ΔR , when seen as functions of T , involve only ΔT . In other words, $\Delta C = C' \Delta T$ and $\Delta R = R' \Delta T$, where $'$ denotes the derivative with respect to T as evaluated at $T = T^{(0)}$. Note that $\Delta T \propto \sin(\omega t)$. As a result, Equation (18) becomes a set of linear ordinary differential equations that can be put in matrix form as

$$\frac{d\Delta f(t)}{dt} = M\Delta f(t) + D\Delta T(t) , \quad (20)$$

where the column vector $\Delta f(t) \equiv [\Delta f_V, \Delta f_{VI}, \dots, \Delta f_{XV}]^T$. The constant coefficient matrix M is a tri-diagonal one, for which the non-zero elements can be readily recognized from the first row on the RHS of Equation (18). On the other hand, the elements in the constant column vector D read

$$D_q = N^{(0)} \left[f_{q-1}^{(0)} C'_{q-1} - f_q^{(0)} (C'_q + R'_q) + f_{q+1}^{(0)} R'_{q+1} \right] . \quad (21)$$

Despite the rather complicated form of M and D , Equation (20) is in fact a textbook problem. In short, its solution, subject to the initial condition that $\Delta f_q(t=0) = 0$, comprises terms that involve either $\exp(\lambda_q t)$ or $\sin(\omega t + \alpha_q)$, where λ_q represents the eigenvalues of the matrix M and α_q represents some phase angle. We find that all values of λ_q are real and distinct, with all but one being negative. Note that one eigenvalue has to be zero because Equation (20) guarantees that $\sum_q \Delta f_q = 0$ at all times. The end result is that as time proceeds, the terms involving $\exp(\lambda_q t)$ with negative λ_q damp out, and the solution becomes sinusoidal. The factors in front of $\exp(\lambda_q t)$ are q -dependent, and therefore the duration it takes for Δf_q to become sinusoidal also depends on q . For instance, the transitory phase for Fe XIV turns out to last for ~ 12 secs. However, for both Fe IX and Fe XII, the transitions to a stationary state both take only about several seconds. And in the transitory phase, Δf_{IX} (Δf_{XII}) turns out to decrease (increase) slightly. All these behaviors are in close agreement with the blue curves in Figure 2. In fact, despite the two simplifying assumptions behind Equation (20), its solution is accurate to within 1.12% (10.6%) for Fe IX (Fe XII).

We now compute the emissivity at each grid point (r, z) at time t via

$$\epsilon = G_{\lambda 0} N^2 , \quad (22)$$

where

$$G_{\lambda 0} = h\nu_{ij} \cdot 0.83 \cdot Ab(\text{Fe}) f_q \frac{n_j A_{ji}}{N} \quad (23)$$

is the contribution function. Here $h\nu_{ij}$ is the energy level difference, $Ab(\text{Fe})$ is the abundance of Fe relative to Hydrogen, f_q is once again the ionic fraction of Fe in ionic state q , n_j is the fraction of Fe in state q lying in level j , and A_{ji} is the spontaneous transition probability. We compute $G_{\lambda 0}$ with the function `g_of_t` in CHIANTI for both Fe IX 171 Å and Fe XII 193 Å. For the ionic fractions (f_q), we consider both the EI and NEI values.

Both the line intensities and spectral profiles depend on the LoS. For convenience, we convert the computed data from the cylindrical to a Cartesian grid where the spacing is 30 km in all three directions. Note that only ϵ , T , v_r , and v_z are needed, and appropriate interpolation is necessary. A

data hyper-cube in $(x, y, z; t)$ results. For each LoS, we consider photons emitted from two squares of different sizes when projected onto the plane of sky. Two sizes are considered, one being 30 km (labeled the “thin” beam hereafter) and the other 720 km (or equivalently 1”, labeled the “thick” beam). For a thin beam, we compute the specific intensity (I) by integrating ϵ with a spacing of 30 km along the LoS. On the other hand, we discretize a thick beam into a series of thin beams, and compute I by summing up the contributions from all individual thin beams⁶. The spectral profiles are found with the same procedure by integrating ϵ_λ at a wavelength λ off line center λ_0 . Following Van Doorselaere et al. (2016), ϵ_λ is given by

$$\epsilon_\lambda = \frac{2\sqrt{2\ln 2}}{\sqrt{2\pi}\lambda_w} \epsilon \exp\left(-\frac{4\ln 2}{\lambda_w^2} (\lambda - \lambda_0 (1 - v_{\text{LoS}}/c))^2\right), \quad (24)$$

where $\lambda_w = (2\sqrt{2\ln 2})\lambda_0(v_{\text{th}}/c)$ is the full-width at half-maximum with v_{th} ($\propto \sqrt{T}$) being the thermal speed determined by the instantaneous temperature. Furthermore, v_{LoS} is the velocity projected onto a LoS, which in turn is found from the instantaneous flow velocity. Similar to AvD13, we take λ to range from $\lambda_0 - 0.07 \text{ \AA}$ to $\lambda_0 + 0.07 \text{ \AA}$ with a spacing of 1.4 mÅ.

4. RESULTS

To start, Figure 3 examines the temporal evolution of the specific intensities of Fe IX 171 Å (the left column) and Fe XII 193 Å (right) for LoS 1 (the top row) and LoS 2 (bottom). For the ease of comparison, these intensities have been normalized by their values at time $t = 0$. The EI (the red curves) results are shown for comparison with the NEI (blue) results, and the effects of different beam sizes are also examined with the results for thin (thick) beams shown by the solid (dotted) curves. Before anything, let us note that the difference between any solid curve and its dotted counterpart is marginal. This agrees with previous results by Gruszecki et al. (2012, see also AvD13) in that a beam size comparable with the half-width of the coronal loop is still adequate for resolving the sausage mode. Note that sausage modes are unlikely to be sensitive to the fine structuring transverse to coronal loops (e.g., Pascoe et al. 2007; Chen et al. 2015a). Note further that coronal loops typically possess apparent widths over a couple of arcsecs (e.g., Aschwanden et al. 2004; Schrijver 2007). In what follows we will discuss only the results pertinent to the thin beams because a resolution of 1” is readily achievable with modern spectrometers like Hinode/EIS (Culhane et al. 2007) and IRIS (De Pontieu et al. 2014).

Whether or not NEI is considered, the intensity variation is consistently stronger for LoS 1 than for LoS 2. This is primarily because LoS 1 samples the portions where the density varies in phase, whereas LoS 2 samples areas where compression and rarefaction are both present (see Figure 1c). In addition, the intensity variation in Fe XII 193 Å is consistently stronger than in Fe IX 171 Å. This comes largely from the opposite temperature dependence of the contribution functions for the two lines. While G increases with T for Fe XII 193 Å, it follows the opposite trend for Fe IX 171 Å. Now that the density N always varies in phase with T , the product $G_\lambda N^2$ and hence ϵ possesses a stronger variation for the Fe XII 193 Å line (see Equation 22).

⁶ We omit the geometric factor $1/4\pi$ when computing I because only the relative variations in I will be examined. Here by “relative variations”, we mean I/I_0 where $I_0 \equiv I(t = 0)$ (see e.g., Figure 3). The plane of sky (PoS) becomes different when we switch from one LoS to another. For both lines of sight, we make sure that the squares are either 30 km or 720 km across when projected onto the respective PoS. It then follows that I/I_0 starts from unity when $t = 0$ by definition. The absolute value of I_0 is indeed different for different lines of sight when the square size is fixed, or for different square sizes along a given line of sight.

Now move on to the effects of NEI. Evidently, for the parameters we choose, introducing NEI enhances the intensity variation for Fe IX 171 Å, whereas the opposite happens for Fe XII 193 Å. This effect is readily seen for LoS 1 (Figs. 3a and 3b), and can also be discerned for LoS 2 (Fig. 3d). To understand why NEI impacts the two spectral lines differently, we take LoS 1 and examine only the interval between 3 and 5 secs, because LoS 2 and other intervals can be understood in the same way. Figure 2 indicates that, in this time interval, the ionic fraction f_{IX} (f_{XII}) is smaller (larger) for EI than for NEI, despite that the overall variations in ionic fractions are consistently stronger when EI is assumed. Given that G_λ is proportional to the ionic fraction, one finds that $G_\lambda N^2$ is smaller (larger) in the EI case for Fe IX (Fe XII).

Figure 4 presents the synthesized spectral profiles for Fe IX 171 Å for both LoS 1 (the upper row) and LoS 2 (lower). Given in the left and middle columns are their temporal evolution when EI and NEI are adopted, respectively. An inspection of these columns indicates that the most obvious difference between the EI and NEI results lies in the temporal variations in the intensity (I_{λ_0}) attained at the rest wavelength λ_0 for LoS 1. While $I_{\lambda_0}(t)$ is enhanced once every half the wave period ($P/2$) for both EI and NEI, the magnitude of the enhancement is nonetheless different when t differs by $P/2$ in the NEI case (Figure 4b). Take $t = P/4 = 1.56$ sec and $t = 3P/4 = 4.66$ sec. The values of I_{λ_0} are approximately the same for EI but show some evident difference for NEI. This behavior can be understood as follows. First, at these instants of time, the fluid velocities are zero along LoS 1, which is actually true for the entire computational domain because $\cos(\omega t) = 0$ (see Equation 2 and 3). The exponential term can then be dropped from Equation (24), and therefore I_{λ_0} becomes a LoS integration of ϵ_{λ_0} that is proportional to ϵ/\sqrt{T} . Now see the contribution function (G_{λ_0}) and consequently the emissivity (ϵ) as functions of electron density (N) and temperature (T) in view of Equations (23) and (22). Define $G_T = \partial G_{\lambda_0}/\partial T$ and $G_N = \partial G_{\lambda_0}/\partial N$, both evaluated at the equilibrium values (N_0, T_0). Define further that $\Delta N = N - N_0$ and $\Delta T = T - T_0$, and recall that $\Delta T/T_0 = (\gamma - 1)\Delta N/N_0$. Despite the specific form of G_{λ_0} , we find that the variation in ϵ_{λ_0} is largely determined by first-order perturbations in N and T . In other words,

$$\frac{\epsilon}{\sqrt{T}} \approx \frac{G_0 N_0^2}{\sqrt{T_0}} \left[1 + \left(\frac{G_N N_0 + (\gamma - 1)G_T T_0}{G_0} + 2 - \frac{\gamma - 1}{2} \right) \frac{\Delta N}{N_0} \right], \quad (25)$$

where G_0 is G_{λ_0} evaluated at (N_0, T_0) . Now that $\Delta N/N_0 \propto \sin(\omega t)$, one finds that the value that ϵ/\sqrt{T} attains at $t = P/4$ ($\sin(\omega t) = 1$) is different from the value at $t = 3P/4$ ($\sin(\omega t) = -1$). Note that while Equation (25) pertains only to a fixed location, the contribution from the first-order terms survives the LoS integration process. As a result, in general I_{λ_0} at these instants of time should be different in both the EI and NEI cases, meaning that, strictly speaking, I_{λ_0} oscillates at the wave period (P) whether or not NEI is considered. It is just that, for Fe IX 171 Å, the difference is not as obvious when EI is adopted, and the reason is that G_N is effectively absent in the EI case but plays a substantial role in the NEI case.

The differences in I_{λ_0} notwithstanding, the spectral profiles are remarkably similar in the EI and NEI results. To quantify this, at each instant of time, we also conduct Gaussian fitting to the instantaneous line profile such that the Doppler velocity and width are derived. These values are presented in the right column as functions of time, and we distinguish between the EI (the red curves) and the NEI cases (blue). For both Lines-of-Sight, NEI does not introduce any appreciable difference to either the Doppler velocity or width. This was anticipated by AvD13 on the basis of Equation (24) given that the ionic fraction enters into discussion only through ϵ , which does not

affect how ϵ_λ depends on λ . However, while this is obvious at any given location, a synthesized spectral profile is in fact a LoS integration, meaning that the relative contributions from emitting materials actually depend on ϵ , which in turn depends on the ionic fraction. The right column of Figures 4 is reassuring in the sense that, at least for the parameters we choose, the spectral profiles of Fe IX 171 Å can indeed be analyzed without invoking the involved NEI effects. The same can be said for Fe XII 193 Å (not shown) as far as the effects of NEI on the Doppler velocities and widths are concerned. In fact, the Doppler velocities and widths found with Fe XII 193 Å are identical to what we have for Fe IX 171 Å.

Compared with NEI, viewing angles play a far more important role in determining Doppler velocities and widths. For LoS 1, the Doppler speed is identically zero (see Figure 4c), which is expected given that the contributions to LoS 1 from outward and inward moving fluid parcels cancel out each other. These bulk motions then contribute to the Doppler broadening, which oscillates at half the wave period ($P/2$, Figure 4d). For LoS 2, however, the LoS velocities survive the integration process, resulting in a Doppler velocity oscillating at the wave period (Figure 4g). These bulk motions (rather than thermal motions) also contribute to the Doppler broadening, which also possesses a period of $P/2$ (Figure 4g).

Then what will be the tell-tale signatures of NEI in observations? The comparison of Figure 3 with 4 indicates that LoS 1 does not help for this purpose, because the intensity and Doppler width signals oscillate with different periods, and a phase-relation analysis is not straightforward. Considering LoS 2, one finds that Fe IX 171 Å is not helpful either because the intensities variations are extremely weak (Fig. 3c). For this LoS, however, one may focus on Fe XII 193 Å and examine the intensity series (Figure 3d) against the Doppler width variations (Figure 4h). For both EI and NEI computations, these two time series possess the same period of $P/2$. Nonetheless, they are 180° out-of-phase provided that Fe is in ionization balance. On the contrary, for the parameters we choose, a phase difference of $\sim 90^\circ$ is seen between the two time series when NEI is incorporated. We note that while both intensity and Doppler width variations are not that strong, they are not undetectable with, say, IRIS (see, e.g., Figure 3 in Tian et al. 2016).

5. SUMMARY

This work was motivated by the notion that, for fast sausage modes in coronal loops, Iron (Fe) may not be able to maintain ionization balance even for relatively dense loop plasmas. To address how non-equilibrium ionization (NEI) affects the modulated emissions, we plugged the self-consistently derived ionic fractions into the contribution functions for both Fe IX 171 Å and XII 193 Å, thereby synthesizing both their specific intensities and spectral profiles. We find that relative to Equilibrium Ionization (EI), NEI plays a far more important role in affecting specific intensities than in determining Doppler velocities or widths. We also find that, for the parameters we choose, NEI may affect the phase-relation between the intensity variations and those in the Doppler widths for Fe XII 193 Å. For lines-of-sight oblique to the loop axis, the two time series possess a phase difference of $\sim 90^\circ$ when NEI is incorporated, whereas the phase difference is 180° when ionization balance is assumed.

Before closing, let us discuss some limitations of the present study and hence the ways to move forward. With a length-to-radius ratio $L/R = 12.5$ and a loop radius $R = 1.5$ Mm, one finds a loop length $L \approx 19$ Mm. While this loop length is not unrealistic, it is nonetheless on the low side of the observed range of the lengths of the EUV loops (see e.g., Figure 1 in Schrijver 2007). Furthermore, while there is observational evidence showing the possible existence of the first longitudinal harmonic

of FSMs in flare loops (e.g., Nakariakov et al. 2003; Melnikov et al. 2005; Srivastava et al. 2008), the observations of higher harmonics in EUV-emitting active region loops have yet to be found. The reason for us to choose a relatively short loop and a higher harmonic is to make sure that the fast sausage mode (FSM) is trapped. As is well-known, FSMs are trapped only when the dimensionless axial wavenumber (kR) exceeds some critical value ($(kR)_{\text{cutoff}}$) (e.g., Edwin & Roberts 1983; Cally 1986; Kopylova et al. 2007). Let n denote the axial harmonic number with $n = 0$ representing the fundamental mode by convention. The dimensionless axial wavenumber kR is then $(n + 1)\pi R/L$. This means that trapped modes are allowed only when n is sufficiently large and/or the loop is sufficiently short. When the plasma beta is small, $(kR)_{\text{cutoff}}$ is largely determined by the density contrast between the loop and its ambient (e.g., Kopylova et al. 2007, Equation 5). We find that $(kR)_{\text{cutoff}} = 0.793$ for the physical parameters we choose, meaning that n needs to be at least three for kR to exceed the critical value for the examined length-to-radius ratio. The fourth harmonic ($n = 4$) is nonetheless chosen, largely compatible with previous forward modeling studies by Gruszecki et al. (2012) and Antolin & Van Doorselaere (2013). The reason for us to stick to the trapped modes is that we would like to avoid further complications associated with the temporal attenuation of the leaky modes. While an eigen-mode analysis is equally possible for both the trapped and leaky modes, the analytically derived eigenfunctions for the leaky ones diverge exponentially in the ambient corona (see e.g., Cally 1986, Equation 3.1). The end result is that, while the periods and damping rates are accurately captured by the eigen-mode analysis, the eigen-functions for the leaky modes cannot fully describe a system experiencing sausage mode oscillations. Rather, the temporal evolution of the system should be examined from the initial-value-problem perspective by using a largely numerical approach (e.g., appendices in Guo et al. 2016; Chen et al. 2016). Consequently the emission properties should be computed with the numerically simulated data. To make our computations as simple as possible, we choose to work with the trapped modes, for which the analytically derived eigen-functions can fully describe a loop oscillating in an eigen-mode.

Having said that, our results can still find applications even to fundamental modes. Firstly, let us consider the case where the fundamental modes are trapped, as would be expected for short and dense flaring loops. Physically speaking, the spatial structures of the perturbations associated with higher longitudinal harmonics are just a repetition of those associated with the fundamental mode (with possible reversal of signs, see Fig. 1). The consequence is that, at sufficiently high spatial resolution, the emission properties for the fundamental mode will be close to our results when one adopts a line of sight that passes through an anti-node. This point was also recognized by Antolin & Van Doorselaere (2013), and employed by Tian et al. (2016) to interpret their IRIS measurements. We are currently conducting a study tailored to this latter work on the Fe XXI 1354 Å emissions modulated by a fundamental FSM. Secondly, the Non-equilibrium Ionization (NEI) effects are expected to be important for fundamental modes even if they are leaky for typical EUV loops. This is because the NEI effects will show up as long as the wave period is not too long when compared with the ionization and recombination timescales. For the fundamental mode, the period (P) is still largely determined by the transverse fast time, and is approximately $(R/v_{\text{Ae}})[2\pi/(kR)_{\text{cutoff}}] \sim 7.1$ secs for the loop examined in this manuscript. This value is rather close to the period of the higher harmonic we examined, for which $P \sim 6.2$ secs. And therefore the deviation of the NEI results from the EI ones are expected. A study on the NEI effects on the EUV emissions associated with a leaky fundamental mode is also underway.

We thank the referee for his/her constructive comments. We thank Drs. Patrick Antolin and Valery Nakariakov for helpful discussions. This work is supported by the National Natural Science Foundation of China (41474149, 41604145, 41674172, 11761141002). TVD is supported by the GOA-2015-014 (KU Leuven) and the European Research Council (ERC) under the European Union's Horizon 2020 research and innovation programme (grant agreement No 724326). ZH is also supported by the Young Scholar Program of Shandong University Weihai (2017WHWLJH07). This work is also supported by the Open Research Program of the Key Laboratory of Solar Activity of National Astronomical Observatories of China (BL: KLSA201801). CHIANTI is a collaborative project involving George Mason University, the University of Michigan (USA) and the University of Cambridge (UK).

REFERENCES

- Antolin, P., De Moortel, I., Van Doorselaere, T., & Yokoyama, T. 2017, *ApJ*, 836, 219
- Antolin, P., & Van Doorselaere, T. 2013, *A&A*, 555, A74
- Aschwanden, M. J., Nakariakov, V. M., & Melnikov, V. F. 2004, *ApJ*, 600, 458
- Banerjee, D., Erdélyi, R., Oliver, R., & O'Shea, E. 2007, *SoPh*, 246, 3
- Cally, P. S. 1986, *SoPh*, 103, 277
- Cally, P. S., & Xiong, M. 2018, *Journal of Physics A Mathematical General*, 51, 025501
- Chen, S.-X., Li, B., Xia, L.-D., & Yu, H. 2015a, *SoPh*, 290, 2231
- Chen, S.-X., Li, B., Xiong, M., Yu, H., & Guo, M.-Z. 2015b, *ApJ*, 812, 22
- . 2016, *ApJ*, 833, 114
- Cooper, F. C., Nakariakov, V. M., & Tsiklauri, D. 2003a, *A&A*, 397, 765
- Cooper, F. C., Nakariakov, V. M., & Williams, D. R. 2003b, *A&A*, 409, 325
- Culhane, J. L., Harra, L. K., James, A. M., et al. 2007, *SoPh*, 243, 19
- De Moortel, I., & Bradshaw, S. J. 2008, *SoPh*, 252, 101
- De Moortel, I., & Nakariakov, V. M. 2012, *Philosophical Transactions of the Royal Society of London Series A*, 370, 3193
- De Pontieu, B., Title, A. M., Lemen, J. R., et al. 2014, *SoPh*, 289, 2733
- Del Zanna, G., Dere, K. P., Young, P. R., Landi, E., & Mason, H. E. 2015, *A&A*, 582, A56
- Edwin, P. M., & Roberts, B. 1983, *SoPh*, 88, 179
- Gruszecki, M., Nakariakov, V. M., & Van Doorselaere, T. 2012, *A&A*, 543, A12
- Guo, M.-Z., Chen, S.-X., Li, B., Xia, L.-D., & Yu, H. 2016, *SoPh*, 291, 877
- Ko, Y.-K., Raymond, J. C., Vršnak, B., & Vujčić, E. 2010, *ApJ*, 722, 625
- Kopylova, Y. G., Melnikov, A. V., Stepanov, A. V., Tsap, Y. T., & Goldvarg, T. B. 2007, *Astronomy Letters*, 33, 706
- Li, B., Chen, S.-X., Xia, L.-D., & Yu, H. 2014, *A&A*, 568, A31
- Melnikov, V. F., Reznikova, V. E., Shibasaki, K., & Nakariakov, V. M. 2005, *A&A*, 439, 727
- Nakariakov, V. M., Hornsey, C., & Melnikov, V. F. 2012, *ApJ*, 761, 134
- Nakariakov, V. M., Melnikov, V. F., & Reznikova, V. E. 2003, *A&A*, 412, L7
- Nakariakov, V. M., & Verwichte, E. 2005, *Living Reviews in Solar Physics*, 2, 3
- Nakariakov, V. M., Pilipenko, V., Heilig, B., et al. 2016, *SSRv*, 200, 75
- Pascoe, D. J., Nakariakov, V. M., & Arber, T. D. 2007, *SoPh*, 246, 165
- Rosenberg, H. 1970, *A&A*, 9, 159
- Ruan, W., He, J., Zhang, L., et al. 2016, *ApJ*, 825, 58
- Schrijver, C. J. 2007, *ApJL*, 662, L119
- Shen, C., Reeves, K. K., Raymond, J. C., et al. 2013, *ApJ*, 773, 110
- Spruit, H. C. 1982, *SoPh*, 75, 3
- Srivastava, A. K., Zaqarashvili, T. V., Uddin, W., Dwivedi, B. N., & Kumar, P. 2008, *MNRAS*, 388, 1899
- Tian, H., Young, P. R., Reeves, K. K., et al. 2016, *ApJL*, 823, L16
- Van Doorselaere, T., Antolin, P., Yuan, D., Reznikova, V., & Magyar, N. 2016, *Frontiers in Astronomy and Space Sciences*, 3, 4
- Yuan, D., & Van Doorselaere, T. 2016, *ApJS*, 223, 23

Zajtsev, V. V., & Stepanov, A. V. 1975,
Issledovaniia Geomagnetizmu Aeronomii i
Fizike Solntsa, 37, 3

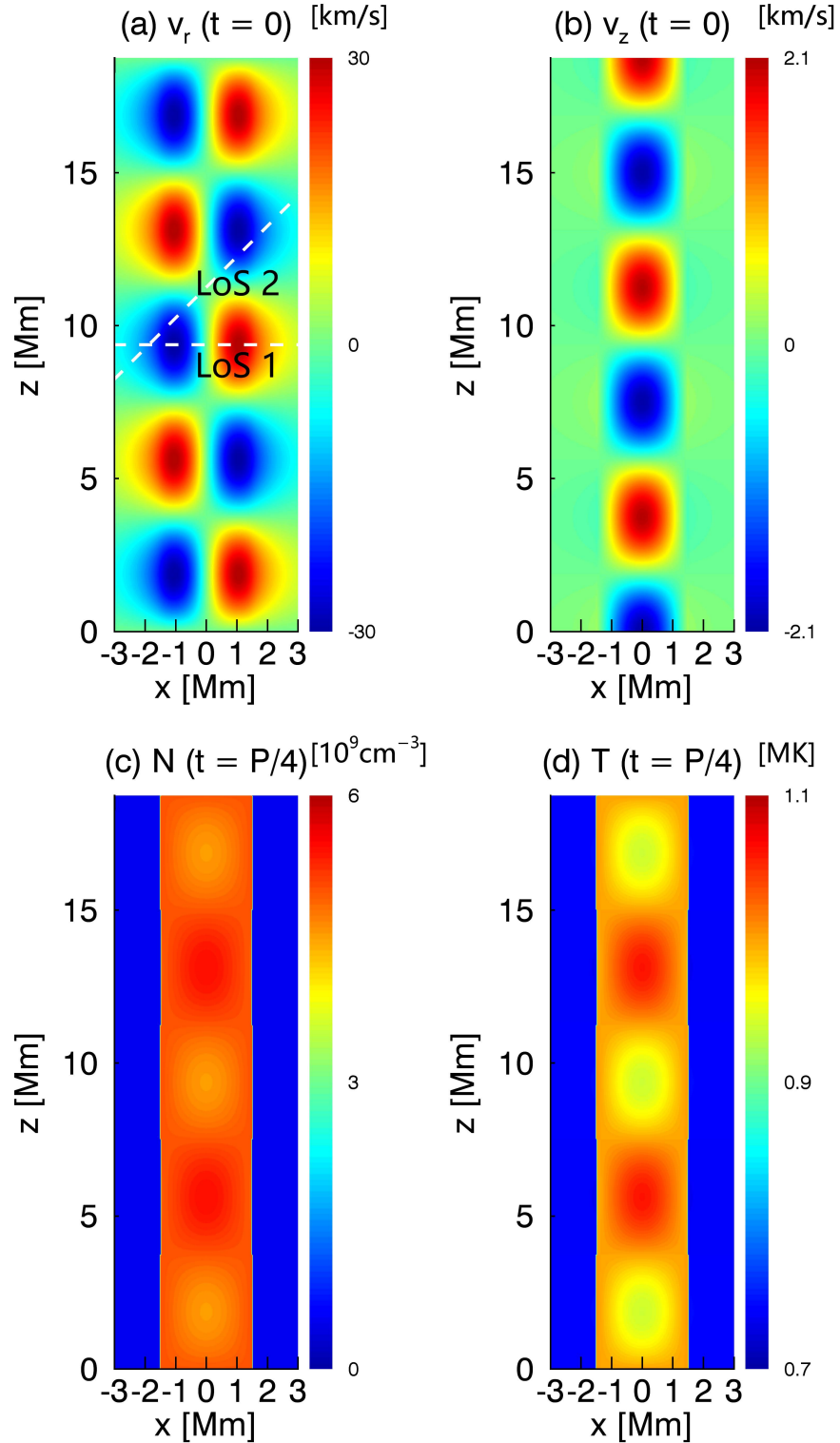


Figure 1. Snapshots of spatial distributions of the flow parameters associated with the fast sausage mode. Shown here is a cut through the cylinder axis. The radial (v_r , panel a) and axial (v_z , panel b) velocities are for $t = 0$, while the electron number density (N , panel c) and temperature (T , panel d) are for t being $1/4$ the wave period. The white dashed lines show the lines-of-sight that this study examines.

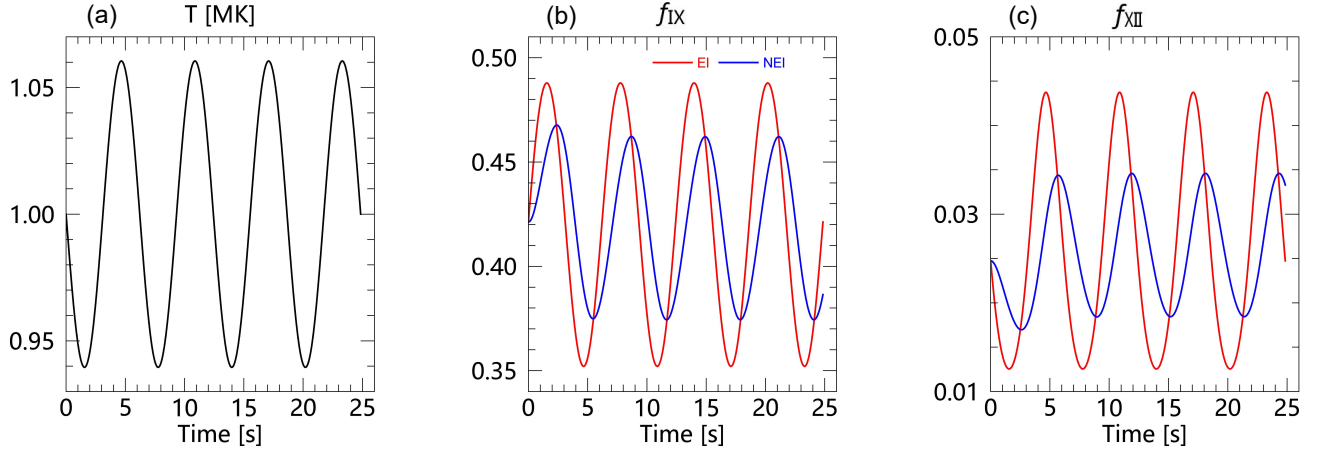


Figure 2. Temporal variations of (a) the electron temperature, (b) the ionic fraction of Fe IX, and (c) that of Fe XII. The values are taken at $[r, z] = [0, L/2]$ with L being the cylinder length, where the compressibility is the strongest. In (b) and (c), the results from the Non-equilibrium-Ionization computation (NEI, the blue curves) are compared with the Equilibrium Ionization (EI, red) results.

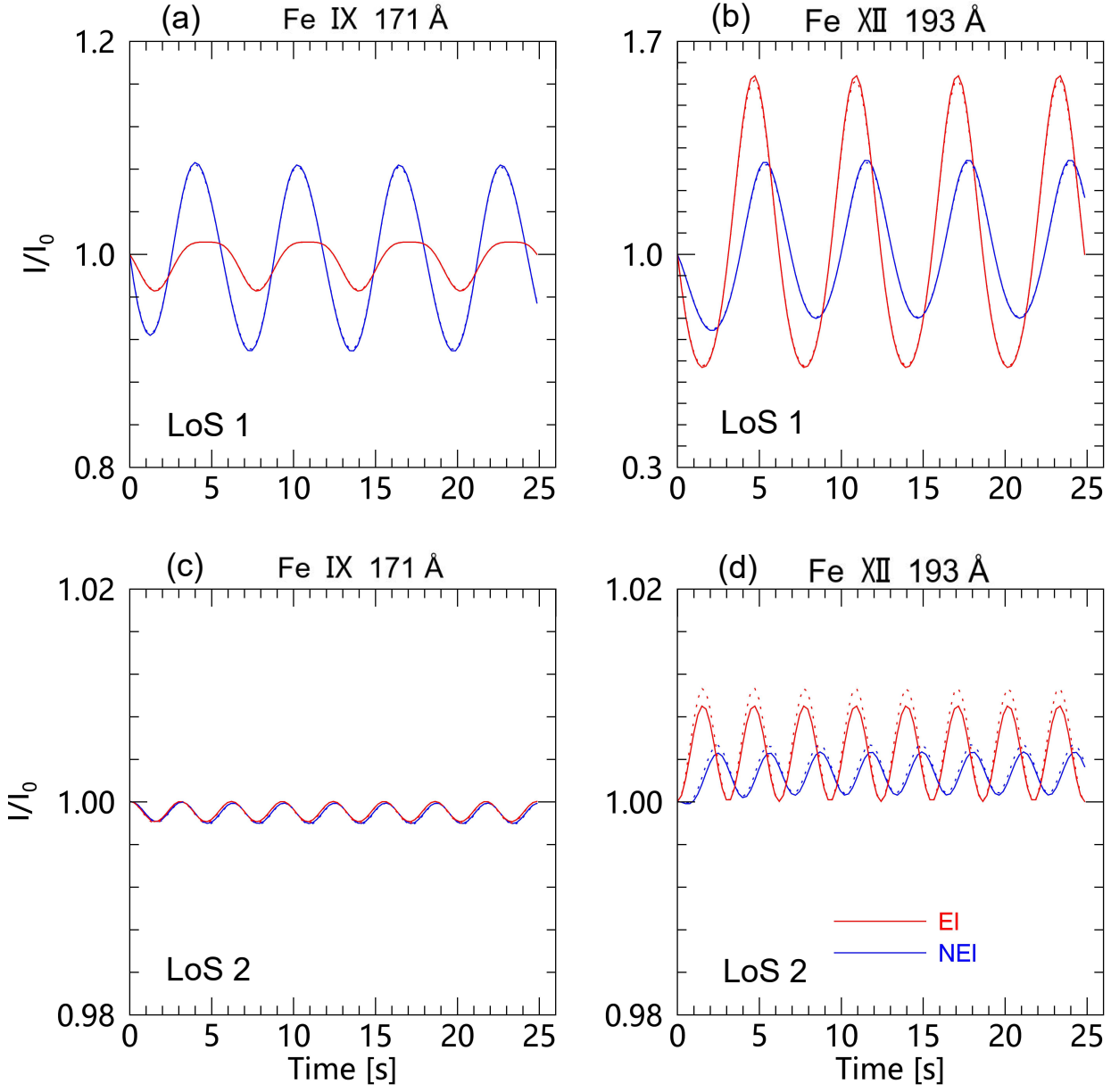


Figure 3. Synthesized specific intensities normalized by their values at $t = 0$ for Fe IX 171 Å (the left column) and Fe XII 193 Å (right). Two LoS, 1 and 2, are examined in the upper and lower rows, respectively. The red and blue lines represent, respectively, the Equilibrium Ionization (EI) and Non-equilibrium Ionization (NEI) results. Furthermore, the solid (dotted) lines are for a beam 30 km (720 km) across when projected onto the plane-of-sky, see text for details.

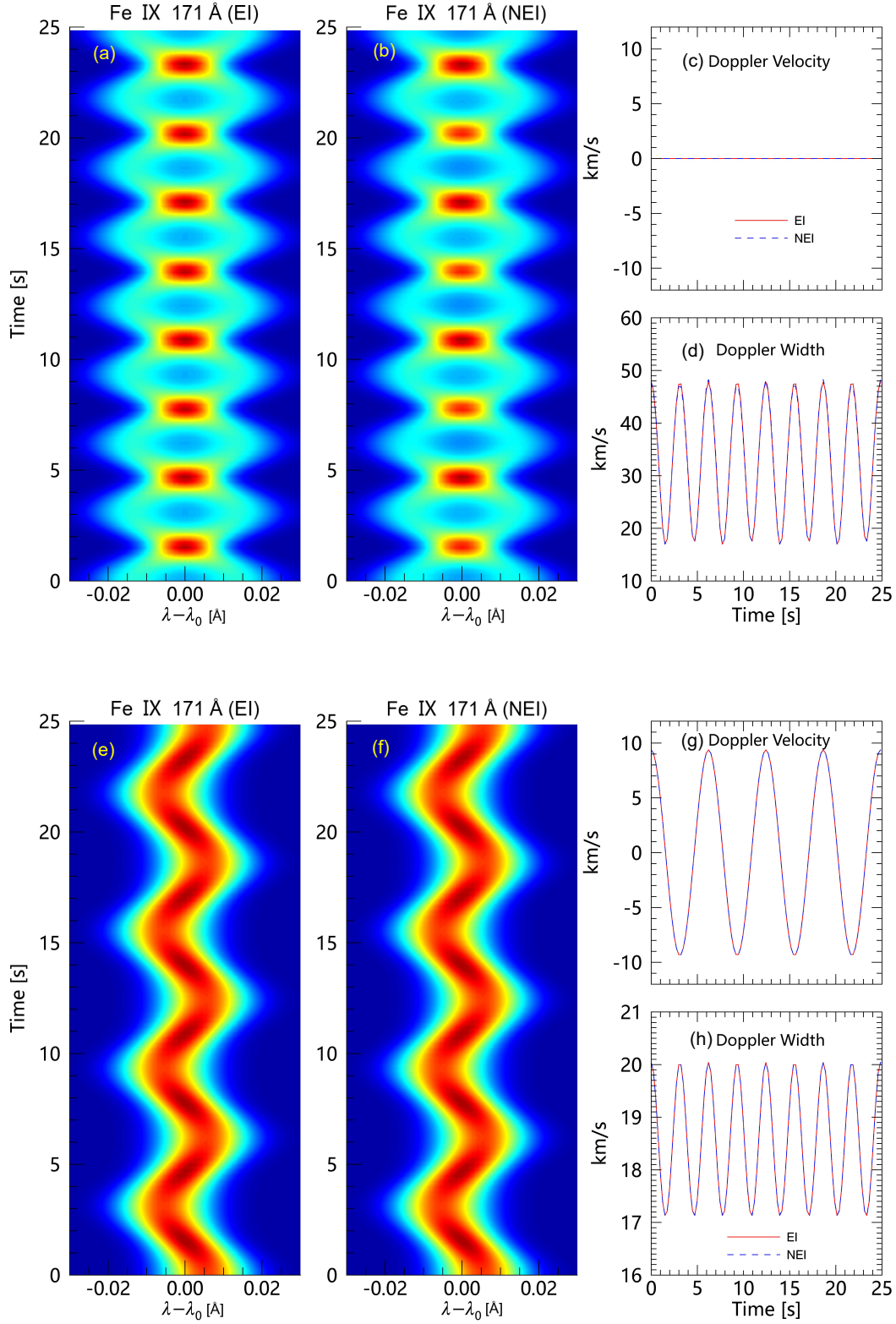


Figure 4. Spectral properties for Fe IX 171 Å along LoS 1 (the upper row) and 2 (lower). The left and middle columns show the spectral profiles when Equilibrium Ionization (EI) and Non-equilibrium Ionization (NEI) are adopted, respectively. In the right column, the Doppler velocity and width are shown for both the EI (the red solid lines) and NEI (blue dashed) cases.